Enhancing Surface Charge Density of Materials

Yong Qin and Qi Xu

Contents

Abstract

With the rapid advancement of wearable electronics, implantable medical devices, Internet of Things, searching appropriate powers for them become urgent. Although the batteries can supply power for them, they suffered the problem of limited capacity and work time. Mechanical energies are ubiquitous either in-vivo or in-vitro. Harvesting these mechanical energies is one of the most promising ways to solve the power crisis for wearable electronics et al. Triboelectric nanogenerators (TENGs) can convert the minor and irregular mechanical energies into electricity. Since their invention in 2012, the TENGs have developed fast and achieved tremendous progress. Nevertheless, there is still a long way to go before it can be commercialized. For the applications of TENGs, improving their output is necessary, otherwise, either supplementary energy

---

Y. Qin (✉) · Q. Xu
Institute of Nanoscience and Nanotechnology, School of Materials and Energy, Lanzhou University, Lanzhou, China
e-mail: qinyong@lzu.edu.cn; xu_qi@lzu.edu.cn

Z. L. Wang et al. (eds.), *Handbook of Triboelectric Nanogenerators*,
https://doi.org/10.1007/978-3-031-05722-9_40-1

storage units or energy costing high precision instruments are needed. The key to improve performance is to improve charge density, as the power of TENG is proportional to the square of the surface charge density of materials. In this chapter, strategies for enhancing the surface charge density of materials are discussed. The contact electrification mechanisms including electron-cloud-potential-well model and flexoelectric polarization model are discussed firstly to explain the charge generation phenomena between different/same friction layers. Then the dynamics of the generated surface charges are discussed to give an inspiration on improving friction layer's charge accommodation capacity. Finally, various methods including materials section, external charges injection, functional group decoration, composite friction layer strategy, working environment utilization are summarized to improve the surface charge density of materials, respectively.

1 Introduction

The wearable electronics, implantable medical devices, and Internet of Things can bring great convenience to the daily life of people, such as health monitoring, assistance to medical treatment, smart agriculture. However, these functional devices are distributed vast, hard to reach, which brings great challenges to the power supply. The traditional power supply methods such as the batteries suffer from the problem of limited capacity and work time, it is time consuming to replace large number of batteries for Internet of Things and will bring about miseries for patients during the replacement of depleted batteries for implantable medical devices. Fortunately, mechanical energies are ubiquitous either in-vivo or in-vitro. If these energies can be harvested, it will provide one of the most promising ways to solve the power crisis for wearable electronics et al.

Most of the ambient mechanical energies are tiny and irregular in frequency and amplitude. Conventional mechanical energy harvesters such as piezoelectric transducer can't be excited by these kinds of mechanical energy and generate electricity further. The triboelectric nanogenerators (TENGs) invented in 2012, give a promising solution to the tiny and irregular mechanical harvesting (Fan et al. 2012a). Based on contact electrification and subsequent electrostatic induction, the mechanical energy can be converted into electricity via displacement current (Wang 2017). The TENGs have the advantage of easy manufacture, low cost. Compared with the piezoelectric transducers, only the electrostatic forces need to overcome during the energy conversion process, so even been driven by the random mechanical forces, TENGs still show a high energy conversion efficiency and have complementary advantages compared with traditional energy harvesting techniques such as electromagnetic induction generator. So far, TENGs can be used to harvest ambient mechanical energy (Zi et al. 2016; Cui et al. 2015; Zhao et al. 2019a) such as wind, body movement, sound, water wave, or as sensors to detect the environment stimuli (Zhao et al. 2019b; Jung et al. 2019).

Nevertheless, there is still a long way to go before it can be commercialized. For the applications of TENGs, improving their output is necessary, otherwise, either supplementary energy storage units or energy costing high precision instruments are needed. As the power of TENG is proportional to the square of the surface charge density of materials, (Zi et al. 2015) so enhancing the surface charge density is important for increasing the power. In this chapter, strategies for enhancing the surface charge density of materials are discussed. The contact electrification mechanisms including electron-cloud-potential-well model and flexoelectric polarization model are discussed firstly to explain the charge generation phenomena between different/same friction layers. Then the dynamics of the generated surface charges are discussed to give an inspiration on improving friction layer's charge accommodation capacity. Finally, various methods including materials section, external charges injection, functional group decoration, composite friction layer strategy, working environment utilization are summarized to improve the surface charge density of materials, respectively.

2 The Origin of Surface Charge during Triboelectrification

In order to improve the surface charge density, we need to know how the surface charge density comes during the electrification process firstly. Generally, the surface charge density can be produced either between the same/different triboelectric materials or by external charge injection. The mechanisms behind these phenomena are different, so we need to analyze them separately.

2.1 Surface Charge Density Originating from Different Materials

Wu et al. used the first principle, calculation to study the electrons transfer process in the microscopic scale (Wu et al. 2018). The Al and PTFE are used as the positive and negative friction materials, respectively. The system reaches an equilibrium state at 2.25 Å (Fig. 1a), which corresponds to a zero-force point and a just-into-contact state. Through Mulliken charge population analysis, the charge profile of Al and PTFE can be obtained, the charge transfer occurs mainly at the interface of the two triboelectric materials (Fig. 1b). Even in the non-contact region, there still exists charge transfer, although with a smaller amount of charge transfer. As the interface distance decreases, the amount of charge transfer increases rapidly (Fig. 1c). This phenomenon can be interpreted by the decreased interface barrier for the electrons transfer from Al to PTFE with the decreasing of interface distance. As the interface distance between Al and PTFE decreases gradually (Fig. 1d), the barrier for electrons transfer decreases, and becomes zero at a distance of 3.6 Å, even they are not in the contact state. Based on the above analyses, the surface micro/nano structures on the surface of triboelectric materials should be designed to obtain an appropriate stress state (interface distance smaller than 2.25 Å) and ensure the increased surface areas

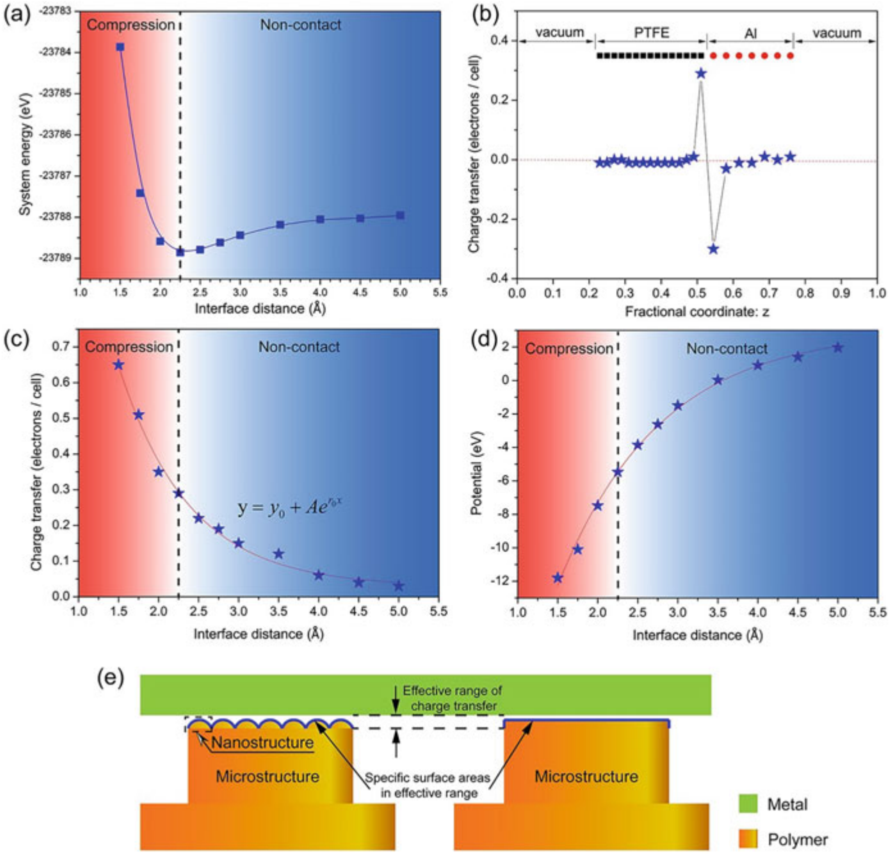

Fig. 1 (**a**) The system energy versus the interface distance between Al and PTFE. (**b**) The charge transfer profile at the interface distance of 2.25 Å. (**c**) The amounts of charge transfer and (**d**) the interface potential at the interface distance from 1.5 Å to 5 Å. (**e**) Schematic of the specific surface areas in effective range of charge transfer (comparison of the polymer with or without nanostructure)

via nanostructures in the effective range of contact electrification (interface distance smaller than 5 Å) to generate more transfer charges.

Xu et al. (2018) tested the real time charge transfer under different temperatures quantitatively through the output of TENGs. The decay behavior of surface charge manifested by the short-circuit transfer charge Q_{sc} with the elated temperature is in accord with the electron thermionic emission model. It is pointed out the electron transfer dominates the contact electrification process. Further, an electron-cloud-potential-well model as shown in Fig. 2a was proposed. When two material contacts gradually under external force, the two single potential wells will emerge and become an asymmetric double potential well, the electrons will transit from the high energy level to the low energy level. In the process of separation, the transited

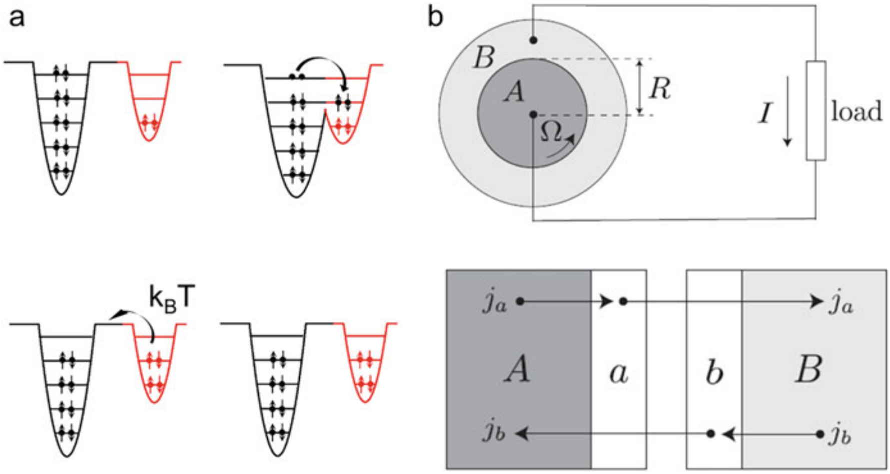

Fig. 2 (**a**) The schematics for explaining contact electrification and charge transfer and release between two materials. (**b)** Schematics of a triboelectric generator when an external motor spins the cylinder of material A and radius R at a sufficient angular velocity Ω with respect to another material B (Alicki and Jenkins 2020)

electrons are blocked from back-flow due to the re-established potential barrier. As the temperature rises up, some of the transited electrons can obtain enough energy to flow back to the material where they come or the air.

In 2020, based on a tight binding Hamiltonian lattice model, a more microscopic theory about the contact electrification are proposed (Willatzen et al. 2020).

$$H = \sum_{l=0}^{N} \left[t_l \left(a_l^{\dagger} a_{l+1} + a_{l+1}^{\dagger} a_l \right) - e\varphi_l a_l^{\dagger} a_l \right] \tag{1}$$

where, H is the Hamiltonian of the system composed of two friction layers in proximity to each other, ls are the labels of the atomic sites, ts are the hopping amplitudes and the strength of the them are controlled by the effective overlap of neighboring atoms, a and a^{+} are the annihilation and creation operators of electrons in the real space, respectively, e is the elementary charge, φ is the electrostatic potential. The hopping amplitude inside the two friction layers are constant. The hopping parameter $t_C(t)$ between two friction layers decreases during the separation process:

$$t_C(t) = t_C \left(\frac{d}{d + vt} \right)^2 \tag{2}$$

By solving the time dependent Schrodinger equation, it showed that the charges on the friction layers shows a quantum mechanical oscillation behavior on the femtosecond to picosecond time scale.

In 2020, based on the theory of bosonic superradiance, Alicki et al. (Alicki and Jenkins 2020) proposed a model for electrification for rotating system as shown in Fig. 2b. The surface electrons of materials A and B are weakly coupled to their corresponding bulk materials, the interactions between the electrons of two surfaces are neglected as they have no contribution to the current generation. Due to the rotation, the surface and bulk electron energy of material A are lowered by an amount of mΩ, where m is the electron mass, Ω is the angular velocity of A. When the Ω is large enough, the pumping rate (B → a) exceeds the corresponding (a → B) decay rate, and this rotation induced popular inversion can serve as the electromotive force to drive the electrons flow in the external load.

2.2 Surface Charge Density Originating from the Same Materials

At the first sight, the charges originated from rubbing the same materials are in conflict with the requirements of symmetry. Early in 1930, Shaw et al. (Shaw and Hanstock 1930) have studied the rubbing of two rods with the same material. One rod is fixed as "rubbed", the other rod is moveable as "rubber" as shown in Fig. 3a. During rubbing, the rubber surface is rubbed always at the same place, the rubbed surface is extended. Due to this asymmetric rubbing, the temperature and strain of the rubber surface increase more quickly than the rubbed. The elated temperature

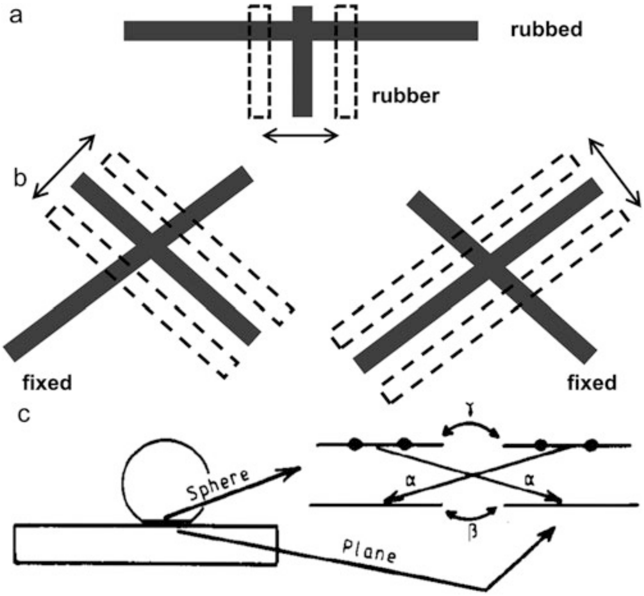

Fig. 3 (**a**) Schematics of the apparatus for electrification testing. (**b**) Two ways of asymmetric rubbing. (**c**) Various kinds of transition considered between the asymmetric contact (Lowell and Truscott 1986)

will facilitate the recovery from strain. As the generated heat during rubbing can dissipate over a larger area in rubbed, so finally the strain in the rubbed will exceeds the rubber. They supposed the strain render negative potential, based on which the potential difference between rubber and rubbed could be well interpreted. In 1953, Henry et al. (Henry 1953) found that the charges could be immediately reversed if the rods are discharged and rubbed again in the opposite sense (Fig. 3b). According to this phenomenon, they inferred it is the temperature gradient across the contact interface induced migration of the charge particles from the hotter part to the cooler part, that makes the same materials triboelectric different during asymmetric rubbing. However, there is not enough experimental data to support this point apart from above mentioned qualitative phenomenon. In 1986, Lowell et al. (Lowell and Truscott 1986) proposed a quantitative model to account for charge generation between identical insulating materials. The models are based on the observation that the electrons are strongly localized in space and energy and have a non-equilibrium distribution. If the two materials are rubbed against each other, the non-equilibrium electrons will gradually encounter the empty state with lower energy and make a tunnel transition across the interface to reach thermal equilibrium. For the asymmetric rubbing as shown in Fig. 3c, the same area of the sphere will lose a small portion of electrons but can pick up more electrons from the extended areas of the plane, which will lead to a net charge transfer. Different from the previous proposed electrification mechanism, it is not necessary to introduce rubbing caused physical difference such as strain and temperature to explain the charge transfer between identical materials. In 2014, Waitukaitis et al. (2014) studied the tribocharging phenomenon for insulating fused zirconium dioxide silicate insulating grains. The experimental results show the large and small grains possess positive and negative charges, respectively. Qualitatively, this phenomenon can be interpreted by the transfer of non-equilibrium trapped electrons upon the grain collisions. However, the measured trapped electrons by thermoluminescence techniques shows their amount is 5 orders smaller than the transferred electrons in the collision experiment. In 2019, Mizzi et al. (2019) pointed out the tribocharging effect comes from the flexoelectric polarization induced by local inhomogeneous strains. The calculated flexoelectric polarizations are generally consistent with the existing triboelectric charge measurements, with feature sizes ranging from the mm to μm range.

2.3 Surface Charge Originating from External Charge Injection

As for most insulators, they can trap charge carriers to form space charge due to the existence of physical and chemical defects such as impurities, defects of the monomeric units, chain irregularities, micro voids, broken bonds. The thermally stimulated current (TSC) is a widely used technique to study the carrier trap nature in the insulating materials. Seggern et al. (von Seggern 1979) identified different traps in the FPA type A foil by TSC. As shown in Fig. 4a, both open circuit and short circuit TSC were used. After the FPA foil is corona charged, there are two peaks located at the 155 °C and 200 °C, respectively as shown from the open circuit TSC (Fig. 4b).

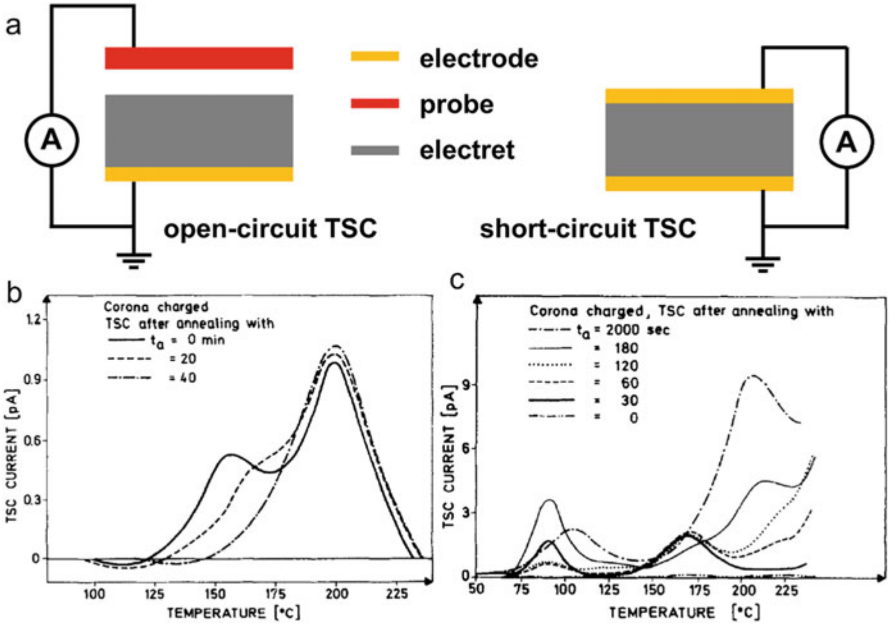

Fig. 4 (**a**) Schematic setup of open- (right) and short-circuit (right) TSC equipment. (**b**) Open-circuit TSC measurements for corona-charged samples after different annealing times (von Seggern 1979). (**c**) Short-circuit TSC measurements of corona-charged and annealed FEP foils (von Seggern 1979)

As for the corona-charged samples, the charges are mainly stored on the surface, which can be ascribed to the low energy of arrived electrons (about 1 eV) travelled through the atmosphere. This can be confirmed by the short circuit TSC as shown in Fig. 4c. None peaks can be found for the unannealed foil, this indicated the charges resides on the surface, as only under these circumstances can the injected charges be compensated by the grounded electrode. After annealed, some trapped carriers are activated and drift toward the inner space. Compared with open-circuit TSC, new peaks located at 95 °C and 170 °C appear, while the peak at 155 °C disappears. It can be concluded the 155 °C represents the surface trap, otherwise it will appear after the foil is annealed. The 170 °C and 200 °C peaks represent the bulk deep trap states, while the 95 °C peak represents the bulk shallow trap state. A further analysis was conducted with the combination of electron-beam charging and open-circuit TSC measurements. The centroid of injected charge by electron beams with different energy were measured by the thermal pulse method (Collins 1975). For the sample charged by electron beams with energy of 3 kV, its TSC spectrum shape is similar to the corona charged one, there exist both 155 °C and 200 °C peaks. The 0.5 μm penetration depth shows the injected charges are distributed near surface.

Based on the penetration depth of electron beams and the TSC results, the geometrical and energetical trap distribution could be analyzed. The 155 °C peak is caused by surface traps with depth ranging from 0.0 μm to 0.5 μm. The 95 °C peak is caused by bulk shallow traps with depth ranging from 0.0 μm to 25 μm. The 170 °C peak is caused by bulk deep traps near the surface with depth ranging from 0.5 μm to 1.8 μm. The 200 °C peak is caused by bulk traps with depth beyond 1.8 μm.

3 The Dynamic Behavior of the Surface Charge Density

As shown in Fig. 5a (Meunier and Quirke 2000), the energy of these traps distributed in a few electron volts from shallow to deep. The depth of an electron trap follows from the corresponding difference in electron affinity. The trap energy of these states is defined by the difference between the electron affinity of the system with and

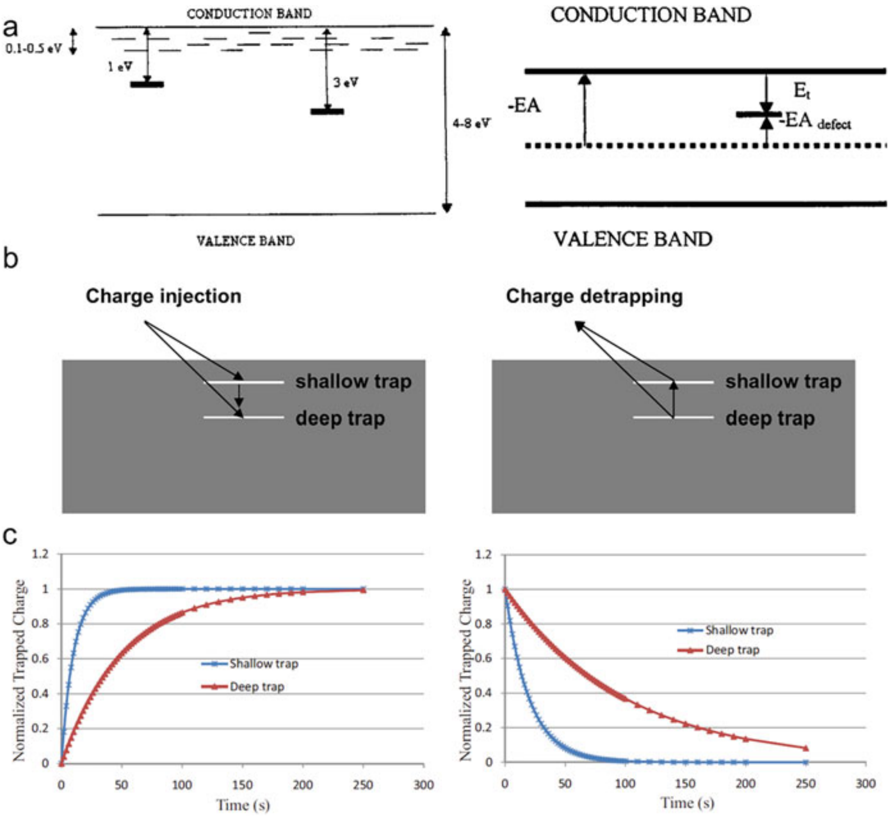

Fig. 5 (**a**) Representation of the band structure of an amorphous polymer. Intraband electron traps are indicated as follows: Shallow traps (physical, <0.5 eV), thin lines, deep traps (chemical, 1–3 eV), thick lines, and the definition of trap energy Et (Meunier and Quirke 2000). (**b**) The schematics of charge trapping processes, and charge detrapping processes. (**c**) Dynamics of charge trapping for shallow and deep traps (Chen and Xu 2009). (**d**) Dynamics of trapped shallow and deep charge during decay (Chen and Xu 2009)

without the defect (Fig. 5a, right). The electron affinity of perfect insulator is the energy consumed to put the electron from vacuum to the conduction band. While the electron affinity of the insulator with defect is the energy needed to place the electrons from vacuum to the defect level. A positive trap energy indicates a potential well for electrons, as the trap has a larger affinity for the electrons. The charges in the dielectrics can be caused by the materials ionization, injection such as tunneling, Schottky injection. In order to understand the trapping process, Chen et al. (Chen and Xu 2009) proposed a two-level model as shown in Fig. 4b. The injected current density J is expressed by,

$$J(E,t) = J_0 \exp\left(\frac{E}{E_0}\right)\left[1 - \exp\left(-\frac{t}{\tau}\right)\right] \tag{3}$$

where J_0 is the initial current when the electric field is E_0, τ is the trapping time constant. The exponentially decay of the current density with time is due to the formation of trapped space charge, which will hinder the injection of charges. For the sake of simplicity, the electron trapping process from the shallow to deep state are not considered. The governing equation for the electron trapping can be expressed by,

$$\begin{aligned} \frac{dn_1}{dt} &= \frac{J\sigma_1}{e}(N_1 - n_1) \\ \frac{dn_2}{dt} &= \frac{J\sigma_2}{e}(N_2 - n_2) \end{aligned} \tag{4}$$

where n_1/n_2, N_1/N_2, σ_1/σ_2 are trapped electrons, total number, the capture cross section of the shallow and deep trap states, respectively, e is the elementary charge. The electron trapping is a dynamic process, it accompanied with the detrapping process. Without consideration of the detrapping from the deep to shallow state, the governing equation for the electron detrapping can be expressed by,

$$\begin{aligned} \frac{dn_1}{dt} &= -k_1 n_1 \\ \frac{dn_2}{dt} &= -k_2 n_2 \end{aligned} \tag{5}$$

where, k_1/k_2 are the thermal detrapping constant of the shallow and deep trap states, respectively,

$$\begin{aligned} k_1 &= N_c v_{th} \sigma_1 \exp\left(-\frac{E_1}{k_B T}\right) \\ k_2 &= N_c v_{th} \sigma_2 \exp\left(-\frac{E_2}{k_B T}\right) \end{aligned} \tag{6}$$

where, v_{th} is the electron thermal velocity, E_1 and E_2 are the trap energy of the shallow and deep state, respectively. Based on the trapping and detrapping kinetics, the changes of total trapped electrons can be expressed by,

$$\frac{dn}{dt} = \frac{J\sigma_1}{q}(N_1 - n_1) - k_1 n_1 + \frac{J\sigma_2}{q}(N_2 - n_2) - k_2 n_2 \tag{7}$$

Supposing σ_1 is larger than σ_2, combined Eqs. (5) and (6), the carrier capture time constant τ_1 is larger than τ_2. The simulated result based on this assumption is shown in Fig. 5c. It can be found the injected charges will fill the shallow trap state with a faster speed. As the charge injection process continues, the ratio of electrons filling the deep traps is larger. As for the detrapping process, compared with shallow trap states, the charges in the deep trap states diminish with a lower speed as shown in Fig. 5d.

The capture cross-section (σ) is conventionally used to characterize the ability of traps to capture carriers, based on the hard-sphere collision model, it can be expressed by,

$$\sigma = \frac{1}{\tau v n} \tag{8}$$

where τ is the carrier capture time constant, v is the carrier thermal velocity, n is the carrier volume density. As for the Si–SiO_2 interface defects, the capture cross section distributes in the range from 10^{-12} to 10^{-23} cm^2. Aiming to these astonishing differences in cross-section, Ryan et al. (2015) pointed out that capture cross section is not a physical property of interface defects. Referring to the charge capture process, both the interface defect state and electron to be captured are initial states. Between the initial state and final state, there exist an activated complex state composed of the interface defect state, the electron to be captured, and phonon. The anticipation of phonons will lead to some structural rearrangement, so it is impossible for the interface defects to remain unchanged during the capturing process. According to the transit state theory (Eyring 1935), the carrier capture time constant τ is,

$$\tau = N_C \frac{k_B T}{h} \exp\left(\frac{-\Delta E}{k_B T}\right) \tag{9}$$

where N_C is the effective density of states in conduction band, k_B is the Boltzmann's constant, T is the temperature, h is the Plank's constant, ΔE is the energy change involved in the capture process. As ΔE is extremely sensitive to how it is measured, combining Eqs. (8) and (9), Ryan et al. pointed out the cross section does not provide meaningful insight into the physics involved. The transition state theory is more appropriate to analyze the charge trapping.

The triboelectric charges generated on the friction layer during the electrification process are not static, it can be neutralized with counter ions in air, or dissipate gradually to the air with the assistance of water (Onogi et al. 1996). In 2016, Cui et al. (2016) studied the dynamic behavior of triboelectric charge dissipated through friction layer to electrode. The electric field in the fiction layer generated by the triboelectric charges and the transferred charges on the electrode will drive the triboelectric charges themselves drift toward the electrode as shown in Fig. 6a. The mobility and intrinsic carriers are two main factors that influence the dynamic

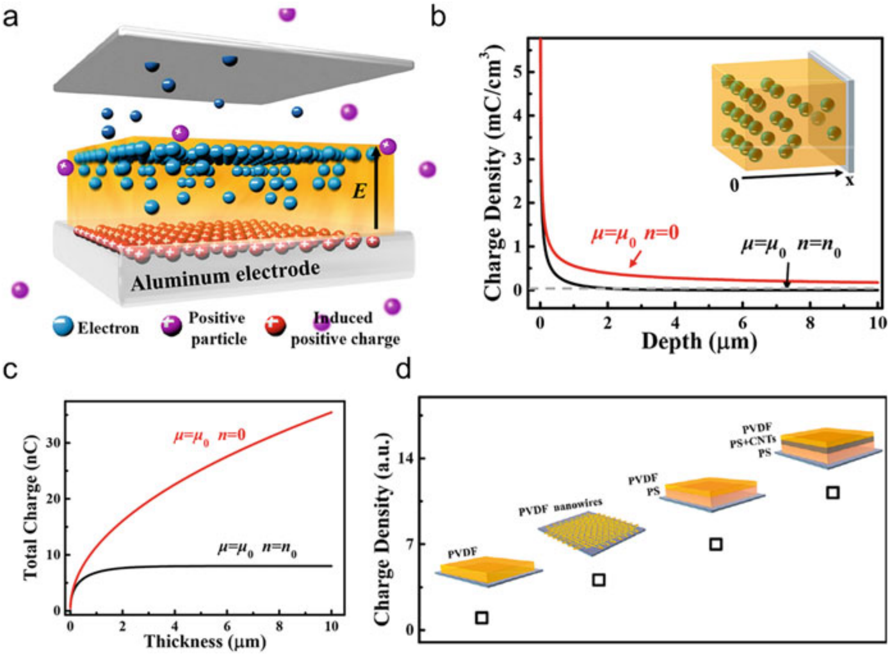

Fig. 6 (**a**) Schematic of the transport process of triboelectric electrons (Cui et al. 2016). (**b**) Theoretical triboelectric charge distribution in the friction layer (Cui et al. 2016). (**c**) Theoretical relationship between the total storage charge and the thickness of the friction layer (Cui et al. 2016). (**d**) Improvement effects of different composite friction layer structure (Cui et al. 2016)

behaviors of triboelectric charges in the friction layer. The intrinsic carriers will recombine with the drifted charges and speed up their attenuation in the friction layer (Fig. 6b). Decreasing the intrinsic carrier can improve the total amount of charges stored in the frication layers effectively (Fig. 6c). Actually, low intrinsic carriers, small carrier mobility, large yield of triboelectric charges are hard to meet simutaneously in one material. According to the dynamic behavior of triboelectric charges, they designed a multi-layered friction structure composed of friction layer, charge collection sublayer, charge transport sublayer, and charge storage and barrier sublayer, the total triboelectric charge density can be improved dramatically (Fig. 6d).

4 Methods to Improve the Surface Charge Density

4.1 Materials Selection

In order to improve the surface charge density during triboelectrification, it needs to select materials with large differences in electronegativity. The triboelectric series can be used to assist the selection of materials as friction layers. The triboelectrification process is susceptible to surface roughness (Persson 2020), humidity (Li et al. 2020) et al., in order to exclude effects caused by these factors, Zou et al. (2019) tested the short-circuit transfer charge between the liquid metal mercury and the polymers in a glove box under fixed temperature, humidity and pressure. The soft and adaptable liquid metal can ensure an intact intimate and a constant pressure with the tested polymers to make the tested results reliable. They use them to quantize the triboelectric series for a wide range of polymers as shown in Fig. 7. Among these polymers, the viton® fluoroelastomer rubber has the largest triboelectric charge density with a value of $-148.2\ \mu\mathrm{C/m^2}$.

Zhang et al. (Zhang and Olin 2020) summarized the materials selection in fabricating TENGs from 100 random selected papers published from 2012 to 2020 as shown in Fig. 8. Among the different negative friction layer materials, polytetrafluoroethylene (PTFE), polydimethyl-siloxane (PDMS), fluorinated ethylene propylene (FEP), and Kapton, are most commonly used materials in fabricating negative friction layers, with percentages of 34%, 22%, 18%, 8%, respectively. Generally, these materials follow their order in the triboelectric series. In the short-circuit condition, the current density can be expressed by,

$$J \approx \sigma_T \frac{dH}{dt} \frac{d_1\varepsilon_0/\varepsilon_1 + d_2\varepsilon_0/\varepsilon_2}{\left(d_1\varepsilon_0/\varepsilon_1 + d_2\varepsilon_0/\varepsilon_2\right)^2} \tag{10}$$

where σ_T is the surface triboelectric charge density, dH/dt represents the contact and separation process of TENGs, ε_0 is the vacuum permittivity, d_1 and d_2 are the thickness of the friction layers, ε_1 and ε_2 are the relative permittivity of the friction layers. From Eq. (10), it can be found that given the triboelectric charge density σ_T, increasing the relative permittivity can also increase the current density. The relative permittivity of metals is very high, so metals are commonly used in fabricating positive fiction layers. Among the different positive friction layer materials, Al, Cu are most commonly used, with percentages of 26%, 20%, respectively.

4.2 Surface Functionalization

Increasing the specific surface area is an effective way to increase the contact area during the electrification process to enlarge the surface charge density of materials. Constructing micro/nanostructures is a general way to increase materials' specific surface area. In 2012, Fan et al. (2012b) fabricated various regular and uniform polymer patterned arrays based on silicon molds and showed that the current density can be increased four times compared with the unstructured films. In 2014, Zheng et al. (2014) used textured electrospun nanofiber as friction layers, the charge increased from 0.085 mC of the smooth friction layers to 0.351 mC, which corresponds to a 4.1 times increase. This result shows that the electrospinning method can achieve the same effect as the other complex patterning methods in increasing the charge density. In 2015, Zhang et al. (2015) developed a one-step plasma etching method to fabricate a large-scale oblique nanowire array on the friction layers (Fig. 9a), and found that

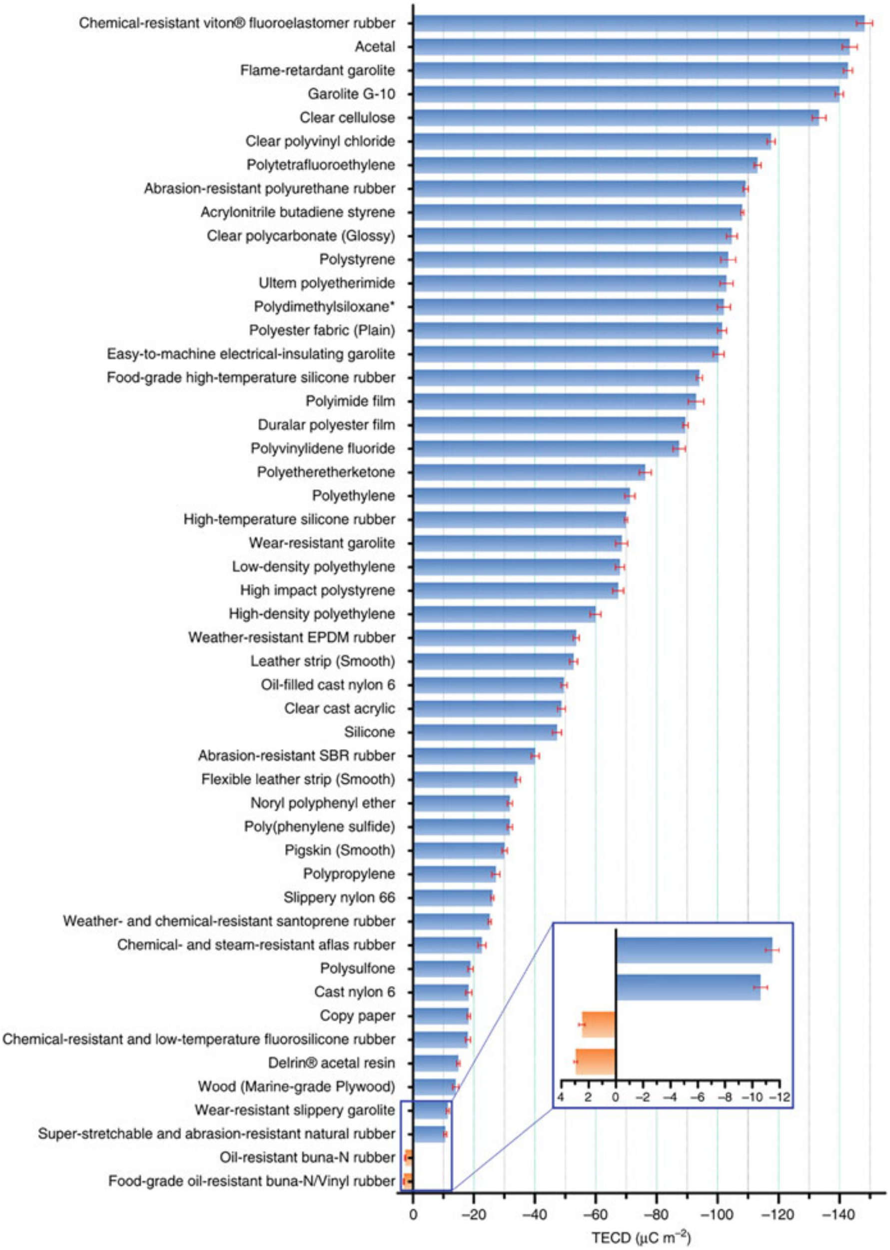

Fig. 7 The quantified triboelectric series (Zou et al. 2019)

compared with the output of TENG composed of vertical nanowire arrays, the charges can increase 2 times (52 nC to 103 nC). This enhancement is due to the oblique NWs are easier to bend and slide during the triboelectrification process and thus generates more triboelectric charges. Besides triboelectrification, surface charge density can also

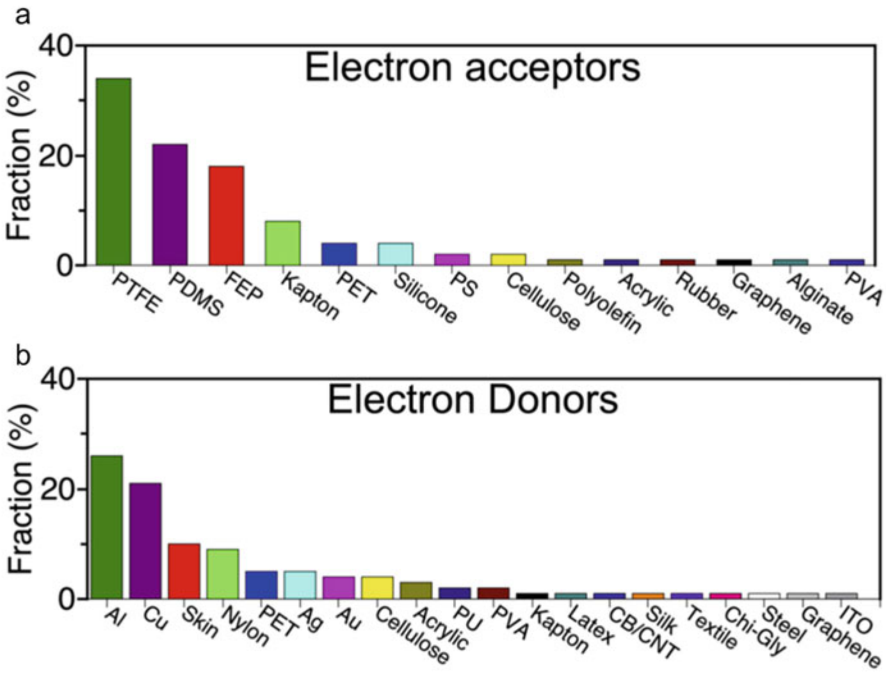

Fig. 8 Fraction (%) of the electron acceptor(**a**), and donor(**b**), materials used in 100 randomly selected articles from 2012 to 2020 (Zhang and Olin 2020)

be increased by external methods. Wang et al. (2014a) found that external charges can be injected into the friction layer to increase the charge density (Fig. 9b). Upon exerting a high voltage on the TENG, the air gap between the pressed friction layers is preferential breakdown due to its small dielectric constant and the generated ionized positive and negative charge will be injected into the friction layers. After the injection, the charge density generated by the TENG increased rapidly from 91 μC/m^2 to 144 μC/m^2 under the voltage of 10 kV (25 V/μm) in the first 2 min and reached a stable value of 148 μC/m^2 after 4 min. During the electrification, the charge transfer between friction layers is mainly determined by their functional groups, so the surface functional group decoration would be a more direct way to increase the surface charge density. Wang et al. (2016) used thiol molecules with different head groups to functionalize Au surfaces, and found that upon contact-electrification with FEP, the amine group can lead to two times increase in surface charge density (Fig. 9c). This enhancement is due to that the amine group has a lower electronegativity.

4.3 Composite Friction Layer

As the triboelectric charges not only exist on the surface of the friction layer, but also can drift toward the inner space of friction layer, fabricating composite friction is an effective way to improve the charge density by making full use of the inner space.

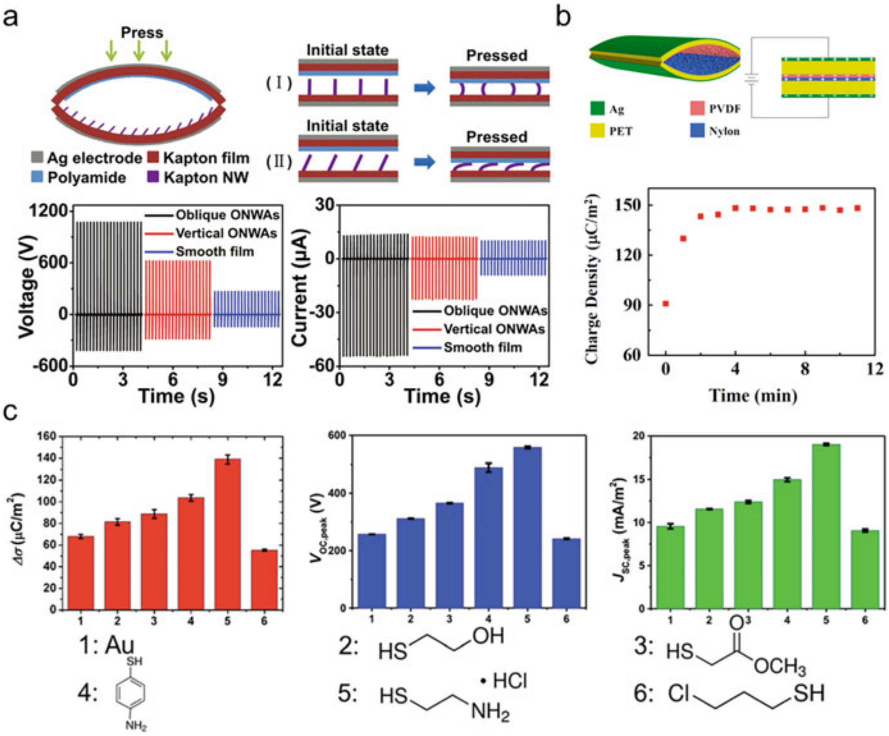

Fig. 9 (**a**) The schematic, working principle, and performance characterization of the TENG composed of oblique ultrafine oblique organic nanowire arrays (Zhang et al. 2015). (**b**) Schematics for the charge injection of TENG and charge density changes with charge injection time under 10 kV injection voltage (25 V/μm) (Wang et al. 2014a). (**c**) Comparisons of the transferred charge density, open-circuit voltage and short-circuit current density for TENG decorated with function groups of 1–6 (Wang et al. 2016)

Cui et al. (2018) designed multi-layered friction structure composed of friction layer, charge collection sublayer, charge transport sublayer, and charge storage and barrier sublayer, for both positive and negative friction layers as shown in Fig. 10a. The charge collection sublayers are used for generating triboelectric charges during the triboelectrification process. The charge collection sublayers are used to transport the triboelectric charge deeper inside to let more entrance of charges. The charge storage and barrier sublayers are used for accommodating the triboelectric charges and protecting them from recombining with the transferred charge through external circuit on the back electrodes. Through this design, the total triboelectric charge density was increased from 0.97 to 160 μC/cm^2. Li et al. (2018) applied the composite friction layer to fiber based TENG as shown in Fig. 10b. The cellulose acetate nanofiber and polyethersulfone were selected as the positive and negative friction layer materials, respectively, due to their stability, flame retardant, and electronegativity difference. The carbon black particle decorated polystyrene nanofibers were served as the charge-transport layer due to the large conductivity of

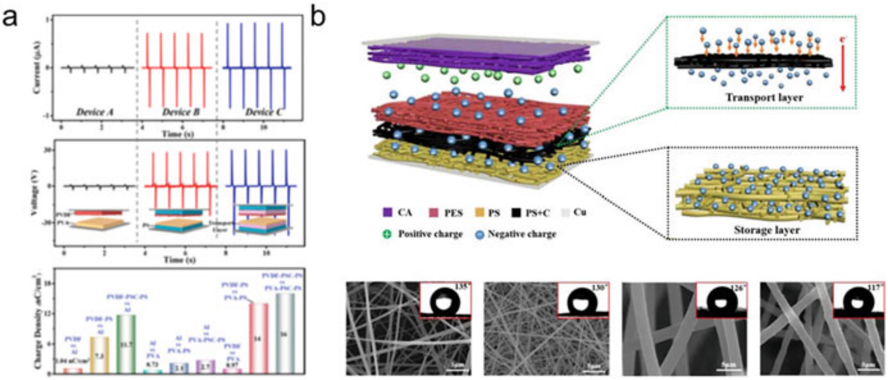

Fig. 10 (**a**) The improvement effects of different composite friction layer structure used in TENG (Cui et al. 2018). (**b**) Schematics of the multilayered fiber-based TENG (Li et al. 2018)

carbon black. The polystyrene nanofibers were selected as the charge-storage layer. The abundant trap levels, small electron mobility and low intrinsic carrier density ensure polystyrene have the ability to hold large enough electrons. Owing to these advantages, the short-circuit current of three-layer structured TENG is 3.07 times the single-layer structured TENG. Chung et al. (2019) developed a composite friction layer composed of charge-generation layer, charge accumulating layer, dielectric layer, and bottom electrode. The electrons in the charge accumulating layer concentrates on the metal-to-metal contact point due to attraction of positive charge in top electrode and repulsion from the electrons in the bottom electrode. When the top electrode gets close to the metal-to-metal contact point, the positive ions exist in the natural atmosphere can reduce the work function of metals, which is beneficial to the air breakdown. Electrons can flow directly to the top electrode, which can notably increase the output power of TENG owing to less energy loss. Through this design, the root mean square can enhance 635% higher compared to conventional TENG.

In addition to the layered composite friction layers, Rana et al. (2021) proposed a poly-DADMAC/nylon-11 composite positive friction layer (Fig. 11a) to improve the output of TENG. The addition of cationic poly-DADMAC to nylon-11 can contribute to the formation of δ’ phase, which possesses a special type of polarization of hydrogen bonds. The polarization of these hydrogen bonds can generate dipoles as shown in Fig. 11b to enhance the nylon-11’s dielectric property. Moreover, poly-DADMAC can trap the free charges in the interface between poly-DADMAC and nylon-11 during the electrospinning process. These charges can induce more dipoles as shown in Fig. 11c, and lead to an increased dielectric constant. As the content of poly-DADMAC filler increase from 0 to 33 wt %, the mat’s dielectric constant increased to 10, which is two times the pristine nylon-11. The further increase of poly-DADMAC will decrease the dielectric constant on the contrary. The interwoven of the composite nanofiber (Fig. 11d) decreases the crystallization in the poly-DADMAC/nylon-11 nanofibers, and the dielectric constant. In addition, the formed conductive path will reduce the inductive charges during the working process of

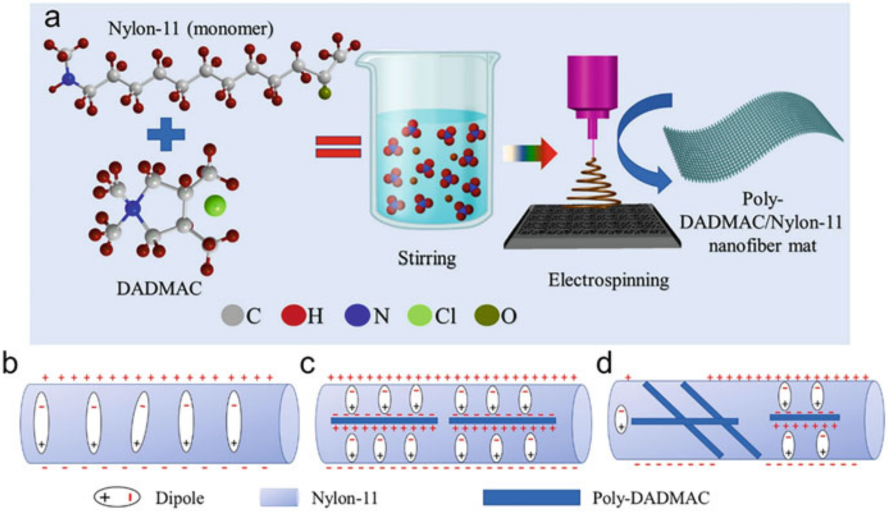

Fig. 11 (**a**) Schematic of the fabrication process and molecular structure of the electrospun poly-DADMAC/nylon-11 nanofiber mat. Schematic of the formation of the dipoles, conduction path, and inductive charges distribution inside the nanofibers mat of (**b**) the pristine polymer, and poly-DADMAC with (**c**) low and (**d**) high filler concentration (Rana et al. 2021)

TENG which is goes against the improvement of output. Under the optimal poly-DADMAC content (33 wt %), the triboelectric charge density can reach 663 μC/m^2.

4.4 Working Environment Optimization

Although improving the charge density can contribute to the improvement of TENG's output, there is an upper limit on the charge density, beyond which, air breakdown will occur and hinder its further improvement. The air breakdown voltage can be empirically described by the Paschen's law,

$$V_b = \frac{APd}{\ln(Pd) + B} \tag{11}$$

where A and B are the constants relevant to the composition and pressure of the gas, P is the gas pressure, d is the gap distance. Under short-circuit, the voltage drop between the gap of friction layers is (Wang et al. 2014b),

$$V_{\text{gap}} = \frac{td\sigma_0}{\varepsilon_0(t + d\varepsilon_r)} \tag{12}$$

where t is the thickness of dielectric layer, d is the gap distance between friction layers, σ_0 is the surface charge density, ε_0 and ε_r are the vacuum permittivity and relative permittivity of dielectric layer, respectively. In order to avoid air breakdown, the V_{gap} should smaller than V_b at any stage during the working process of TENG.

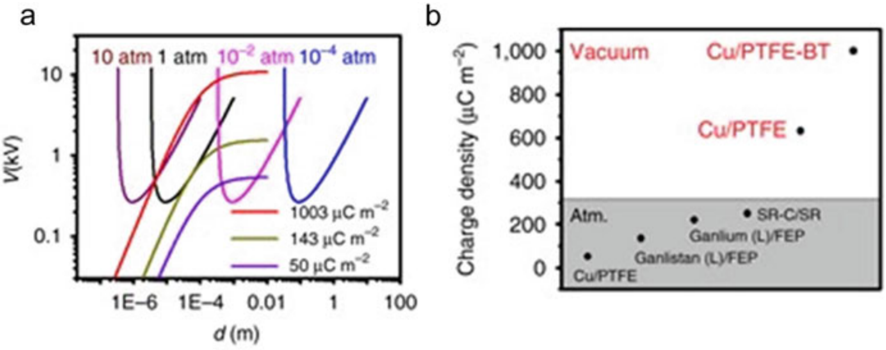

Fig. 12 (**a**) Air breakdown voltage at different pressures and gap voltage of TENG with different charge densities. (**b**) Comparison of the output charges density measured in this work with previously reported ones (Wang et al. 2017)

Wang et al. (2017) studied the performance of TENG under vacuum. As shown in Fig. 12a, both increasing and decreasing the gas pressure to a large degree can contribute to the improvement of surface charges. However, the high gas pressure environment suffers from the latent danger such as explosion, constructing low pressure work environment is more practical. When the working pressure is decreased to 10^{-6} torr, the maximum charge density can reach 1003 $\mu C/m^2$ without air breakdown (Fig. 12b).

The KPFM measures the contact potential difference (V_{CPD}) between the tip and sample (Melitz et al. 2011):

$$V_{CPD} = \frac{\varphi_{\text{tip}} - \varphi_{\text{sample}}}{-e} \tag{13}$$

where e is the elementary charge, φ_{tip} and φ_{sample} are the work function of the tip and sample, respectively. The energy level of the tip and sample is shown in Fig. 13. When the tip and sample are far apart and not electrically connected (Fig. 13a), their fermi levels are different but share a common vacuum level. In electrically equilibrium (Fig. 13b), the fermi levels are aligned, charges of equal quantity and different sign emerge on the surface of tip and sample due to the electron tunneling, the vacuum level are no longer the same, a contact potential difference builds up and produce an electrostatic force. This force can be nullified by applying a bias voltage between the tip and sample with an equal magnitude as V_{CPD} but with opposite sign (Fig. 13c). Applying an AC voltage (V_{AC}) as well as a DC voltage (V_{DC}) to the AFM tip, the resulting electrostatic force is,

$$\begin{aligned} F = &-\frac{\partial C(z)}{\partial z} \\ &\times \left[\frac{1}{2}(V_{DC} - V_{CPD})^2 + (V_{DC} - V_{CPD})V_{AC}\sin(\omega t) - \frac{1}{4}V_{AC}^2(\cos 2\omega t - 1)\right] \end{aligned} \tag{14}$$

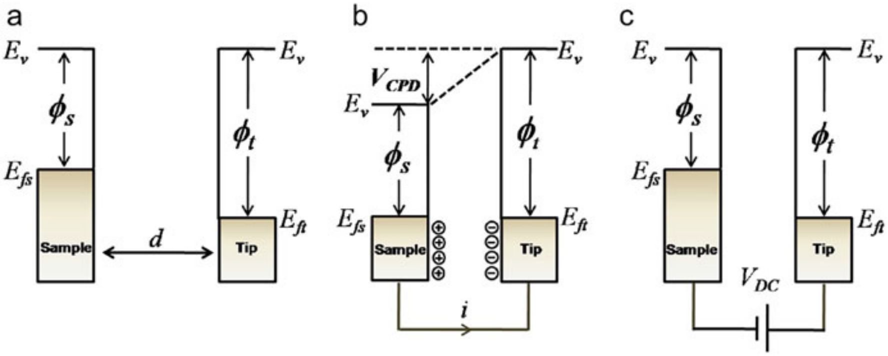

Fig. 13 Electronic energy levels of the sample and AFM tip for three cases: (**a**) tip and sample are separated by distance d with no electrical contact, (**b**) tip and sample are in electrical contact, and (**c**) external bias V_{DC} is applied between tip and sample to nullify the CPD and, therefore, the tip–sample electrical force. E_V is the vacuum energy level. E_{fs} and E_{ft} are Fermi energy levels of the sample and tip, respectively (Melitz et al. 2011)

where $C(z)$ is the capacitance between the tip and sample surface, ω is the angular frequency of the AC voltage. A lock-in amplifier is used to extract the electrostatic force signal with frequency ω, nullifying this signal by tuning the DC voltage, the V_{CPD} can be measured.

As for the contact triboelectrification, besides work function difference, the triboelectric charge induced potential difference is also included. As the work function of the material is constant, the variations of the potential difference can reflect the triboelectric charge, the specific relationship can be expressed by (Zhou et al. 2013):

$$\sigma = \frac{\Delta V_{CPD}\varepsilon_0\varepsilon_r}{t} \tag{15}$$

where, ε_0 is the vacuum permittivity, ε_r is the relative dielectric constant of the sample, t is the thickness of the sample. After an area of 4 × 4 μm (Zhou et al. 2013) was rubbed by an AFM tip operated under contact mode with a normal contact force, the surface topography shows no detectable changes, while the rubbed area shows a potential 0.167 V lower than the intact area (Fig. 14a, b). According to Eq. (15), the contact area of the SiO_2 sample has a negative charge density of $-29\ \mu C/m^2$. To verify the accuracy of this equation, an FEM simulation was conducted (Fig. 14c). Setting the rubber area with a charge density of $-29\ \mu C/m^2$, when a bias voltage of -0.168 V was exerted on the tip, the potential difference between the tip and rubber area became zero. This voltage agrees quite well with the measured voltage of -0.167 V.

Lin et al. (2019) studied the electron transfer in the nanoscale taking the temperature difference between friction layers into consideration. Charge transfer between metal and dielectric was investigated by atomic force microscopy (AFM) and Kelvin probe force microscopy (KPFM). The test was conducted in the AFM platform, and

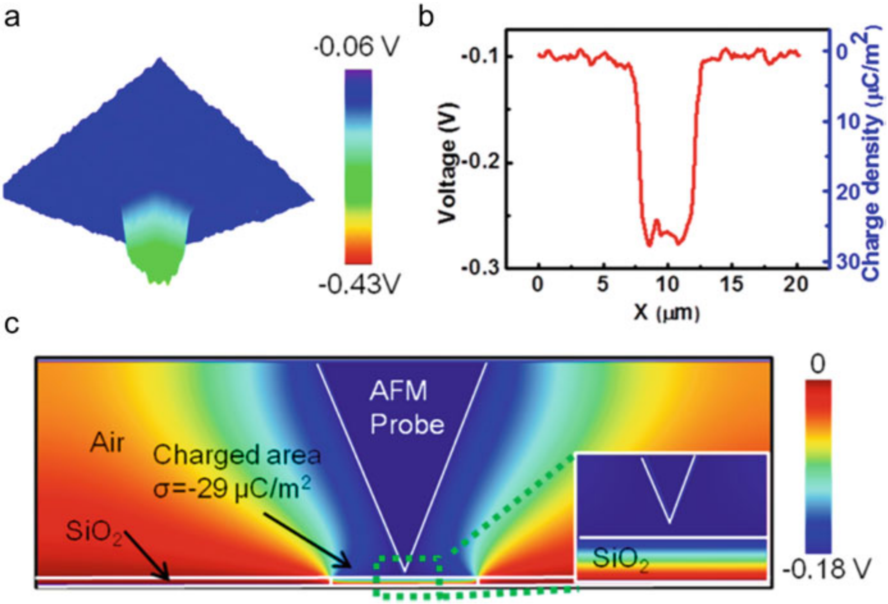

Fig. 14 (**a**) 3D image of the measured surface potential profile. (**b**) Cross section profile of the potential distribution. (**c**) Simulated electric potential distribution in vertical direction under the condition when surface potential was measured in SKPM. Parameters used in simulation: the apex angle of the AFM probe was set to 35° with a tip radius of 10 nm, and had potential of −0.168 V; the center 4 μm area on top surface of SiO_2 had surface charges with a density of −29 μC/m^2, and the bottom surface of SiO_2 was grounded. The inset is an enlarged picture of the tip area (Zhou et al. 2013)

the environmental chamber was filled with Ar. The temperature of tip metal and insulator dielectrics was controlled separately to allow temperature difference between them. The temperature of tip was controlled by tip heater, the temperature of dielectric was controlled by the sample heater. To avoid the friction heating, abrasion, and heat exchange between metal and dielectrics, the AFM worked at the peakforce tapping mode instead of contact mode. In this mode, the contact between the AFM tip and dielectric contact belongs to vertical point contact with a duration of 1 ms, which can effectively prohibit the abrasion and heat exchange. Firstly, keep the tip and dielectric sample at the same temperature, the contact electrification was performed at different temperatures. Based on the KPFM image of the dielectric samples and Eq. (15), the triboelectric charges can be calculated. The SiO_2 sample was negatived charged when being rubbed with the Au coated tip. As the temperature rise, the triboelectric charges gradually decrease, and diminish at temperature 513 K. The contact electrification is a dynamic process. When the tip approaches the SiO_2 dielectric sample, the electrons transferred from the tip to SiO_2. With the separation of the tip and SiO_2 dielectric, part of the received electrons tunnels back to tip or dissipates to air by thermal excitation. As the temperature rise, more electrons will tunnel back or dissipate, so the triboelectric charge decreases correspondingly. When stopping the contact electrification, the triboelectric charge gradually dissipated. However, contrary to the proposed thermionic-emission dissipation model,

$$\sigma = \exp(-\alpha t)\sigma_0 \tag{16}$$

where α is the decay coefficient including temperature, Richardson constant, t is the time, σ_0 is the initial triboelectric charge after stopping the rubbing. In the low temperature range, some of the triboelectric charge seems permanent. The following formula can be used to describe the dissipation behavior of the triboelectric charge,

$$\sigma = \exp(-\alpha t)\sigma_e + \sigma_p \tag{17}$$

where, σ_e is the triboelectric charges reside in the shallow traps, σ_p is the triboelectric charges reside on the deep traps. In the low temperature range, the σ_p are not excited, so this part of triboelectric charges seems permanent. This thermionic-emission dissipation model fits the experiment data very well. Due to the thermionic emission behavior in contact electrification was demonstrated, it is possible to increase the electron transfer by increasing the temperature difference between the tip and dielectric sample. Keeping the temperature of dielectric sample fixed, the triboelectric charge of the dielectric sample increases linearly in temperature range from 313 to 433 K. When the temperature of the tip increases, more electrons will be thermally excited and transfer to the dielectric sample. As the temperature of dielectric sample keeps fixed, the amount of electron tunneling back or dissipated remains unchanged. These two effects contribute to the increase of the triboelectric charges on the dielectric sample.

In practical, under the temperature difference environment, the cooler friction layer can't maintain its temperature fixed due to the heat exchange. So, the influence of temperature on the output of TENGs is a complex process. Cheng et al. (2021) designed a temperate difference based TENG by taking the dissipation of electrons from the cooler friction layer under heat exchange with hotter friction layer into account. A modified electron thermionic emission model was proposed,

$$\sigma_0 = -C_1 T_h + C_2 \tag{18}$$

$$\sigma = \exp(-SAt_0)\sigma_0 \tag{19}$$

$$S = \frac{\lambda_1 A_0}{k_B} T_c \exp\left(\frac{qV}{k_B T_c}\right) \tag{20}$$

where σ_0 is the charge density when the temperature of the cooler friction layer keeps fixed, C_1 and C_2 are material related constants, σ is the charge density taking the temperature change of the cooler friction layer into account, A is the surface area of TENG, t_0 is the time of heat preservation, λ_1 is the material related constant, A_0 is the Richardson constant, k_B is the Boltzmann constant, T_c is the temperature of cooler friction layer. As the temperature of the hotter friction layer rises, the temperature of

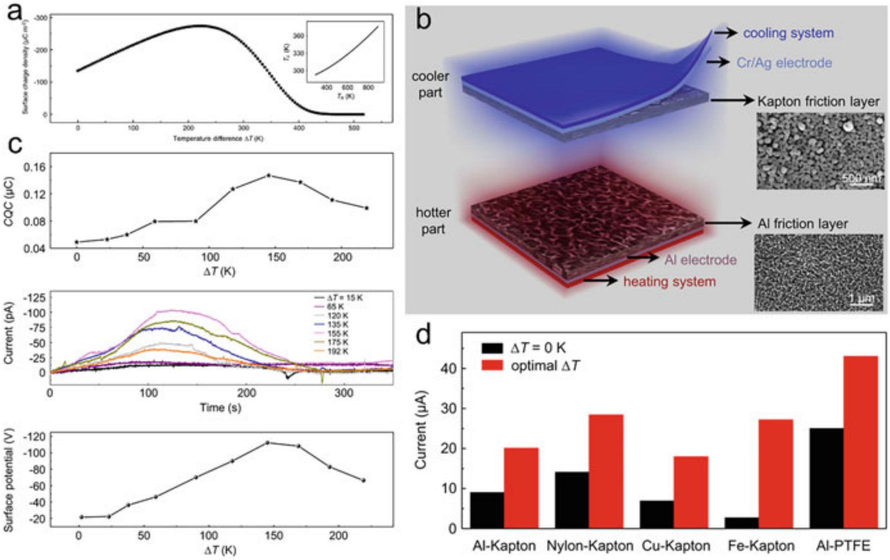

Fig. 15 (**a**) Numerical simulations of the relationship between temperature difference (ΔT) and the triboelectric charge density. The relationship between the temperature of the hotter friction layer (T_h) and the temperature of the cooler friction layer (T_c) is shown in the inset. (**b**) Schematic diagram of TDNG. Insets are scanning electron microscope images of nanostructures on Kapton and Al. (**c**) The relationship triboelectric charge and ΔT; The thermally stimulated discharge current of Kapton after friction at different ΔT; The surface potential of Kapton after friction at different ΔT. (**d**) Short-circuit current with different friction materials when ΔT = 0 K (black column) and optimal ΔT (red column) (Cheng et al. 2021)

the cooler friction also increases as shown in Fig. 15a. On the one hand, the increase of hotter friction layer will thermally excite more electrons and contribute to the charge transfer between friction layers. On the other hand, the temperature of the cooler friction layer will rise due to the heat exchange during the contact separation process; this would cause the electrons in the friction layer tunneled back to the hooter friction layer or escaped to the air, which will decrease the transferred charge across the friction layer. So, there exist an optimal temperature difference between hotter and cooler friction layers under which the TENG has the optimal output as shown in Fig. 15a. This is different from the linear increase in triboelectric charge with the temperature difference in the nanoscale case.

After demonstrating this, they fabricate a temperature difference TENG. As shown in Fig. 15b, the friction layers of the hotter and cooler part are chemical reactive etched Al foil and reactive ion etched Kapton film, respectively. The temperature of the hotter and cooler friction layers is controlled by a thermostat heater and a water-cooling system, respectively. Driven by a linear motor with frequency of 0.7 Hz, the triboelectric charge obtained by integrating the short-circuit current in one period. The triboelectric charge increases first and reaches its peak value of 147 nC (corresponding to a surface charge density of 58.8 μC/m^2) under the temperature difference of 145 K, and then decreases, and this has also been confirmed by the TSD test and surface potential test (Fig. 15c). Under the optimal temperature difference 145 K, the open-circuit voltage, short-circuit current, surface charge density and output power of the TENG are 2.7, 2.2, 3.0, and 4.9 times the TENG with equal temperature. This scheme using the temperature difference to improve the output of TENG can also be extended to other friction layer pairs such as Nylon-Capton, Cu-Kapton, Fe-Kapton, Al-PTFE (Fig. 15d).

5 Conclusion

In this section, a brief introduction about enhancing the surface charge density of materials is given. The electrification mechanism of materials is discussed. The electron transfer dominates the electrification. The electron-cloud-potential-well model and flexoelectric polarization generated during contact can explain the electrification between different/same friction layers. The triboelectric charges not only exist on the surface of the friction layer, but also can drift toward the inner space of friction layer. Decreasing the intrinsic carriers and carrier mobility can improve friction layer's accommodation capacity for triboelectric charges. By testing the short-circuit transfer charge between the liquid metal and the polymers, the triboelectric series for a wide range of polymers are given quantitatively. Based on this series, one can select materials with large differences in electronegativity to achieve large surface charge density. By functionalizing the material surface with micro/nano structure pattern, external charges injection, functional group decoration, the surface charge density can be increased by increasing the contact area or enlarging the differences of electronegativity between friction layers during contact electrification. By adopting composite friction layer strategy, surface charge density can be improved by accommodating more triboelectric charges in the friction layer or triggering field emission. By decreasing the gas pressure, constructing temperature difference, the surface charges can be improved by possessing a more tolerance to air breakdown, improving the electrons transfer between friction layers, respectively.

References

Alicki R, Jenkins A (2020) Quantum theory of triboelectricity. Phys Rev Lett 125(18):186101

Chen G, Xu Z (2009) Charge trapping and detrapping in polymeric materials. J Appl Phys 106(12):123707

Cheng B, Xu Q, Ding Y, Bai S, Jia X, Yu Y, Wen J, Qin Y (2021) High performance temperature difference triboelectric nanogenerator. Nat Commun 12(1):4782

Chung J, Heo D, Shin G, Choi D, Choi K, Kim D, Lee S (2019) Ion-enhanced field emission triboelectric nanogenerator. Adv Energy Mater 9(37):1901731

Collins RE (1975) Distribution of charge in electrets. Appl Phys Lett 26(12):675–677

Cui N, Gu L, Liu J, Bai S, Qiu J, Fu J, Kou X, Liu H, Qin Y, Wang ZL (2015) High performance sound driven triboelectric nanogenerator for harvesting noise energy. Nano Energy 15:321–328

Cui N, Gu L, Lei Y, Liu J, Qin Y, Ma X, Hao Y, Wang ZL (2016) Dynamic behavior of the triboelectric charges and structural optimization of the friction layer for a triboelectric nanogenerator. ACS Nano 10(6):6131–6138

Cui N, Liu J, Lei Y, Gu L, Xu Q, Liu S, Qin Y (2018) High-performance triboelectric nanogenerator with a rationally designed friction layer structure. ACS Appl Energy Mater 1(6):2891–2897

Eyring H (1935) The activated complex in chemical reactions. J Chem Phys 3(2):107–115

Fan FR, Tian ZQ, Wang ZL (2012a) Flexible triboelectric generator! Nano Energy 1(2):328–334

Fan F-R, Lin L, Zhu G, Wu W, Zhang R, Wang ZL (2012b) Transparent triboelectric Nanogenerators and self-powered pressure sensors based on micropatterned plastic films. Nano Lett 12(6):3109–3114

Henry PSH (1953) The role of asymmetric rubbing in the generation of static electricity. Br J Appl Phys 4(S2):S31–S36

Jung YH, Hong SK, Wang HS, Han JH, Pham TX, Park H, Kim J, Kang S, Yoo CD, Lee KJ (2019) Flexible piezoelectric acoustic sensors and machine learning for speech processing. Adv Mater 32(35):1904020

Li Z, Zhu M, Qiu Q, Yu J, Ding B (2018) Multilayered fiber-based triboelectric nanogenerator with high performance for biomechanical energy harvesting. Nano Energy 53:726–733

Li L, Wang X, Zhu P, Li H, Wang F, Wu J (2020) The electron transfer mechanism between metal and amorphous polymers in humidity environment for triboelectric nanogenerator. Nano Energy 70:104476

Lin S, Xu L, Xu C, Chen X, Wang AC, Zhang B, Lin P, Yang Y, Zhao H, Wang ZL (2019) Electron transfer in nanoscale contact electrification: effect of temperature in the metal-dielectric case. Adv Mater 31(17):1808197

Lowell J, Truscott WS (1986) Triboelectrification of identical insulators. II. Theory and further experiments. J Phys D Appl Phys 19(7):1281–1298

Melitz W, Shen J, Kummel AC, Lee S (2011) Kelvin probe force microscopy and its application. Surf Sci Rep 66(1):1–27

Meunier M, Quirke N (2000) Molecular modeling of electron trapping in polymer insulators. J Chem Phys 113(1):369–376

Mizzi CA, Lin AYW, Marks LD (2019) Does flexoelectricity drive triboelectricity? Phys Rev Lett 123(11):116103

Onogi Y, Sugiura N, Nakaoka Y (1996) Dissipation of triboelectric charge into air from textile surfaces. Text Res J 66(5):337–342

Persson BNJ (2020) On the role of flexoelectricity in triboelectricity for randomly rough surfaces. Europhys Lett 129(1):10006

Rana SMS, Rahman MT, Sharma S, Salauddin M, Yoon SH, Park C, Maharjan P, Bhatta T, Park JY (2021) Cation functionalized nylon composite nanofibrous mat as a highly positive friction layer for robust, high output triboelectric nanogenerators and self-powered sensors. Nano Energy 2021(88):106300

Ryan JT, Matsuda A, Campbell JP, Cheung KP (2015) Interface-state capture cross section—why does it vary so much? Appl Phys Lett 106(16):163503

Shaw PE, Hanstock RF (1930) Triboelectricity and friction. V. on surface strain and relaxation of like solids. Proc R Soc London A 128(808):474–480

von Seggern H (1979) Identification of TSC peaks and surface-voltage stability in Teflon FEP. J Appl Phys 50(4):2817–2821

Waitukaitis SR, Lee V, Pierson JM, Forman SL, Jaeger HM (2014) Size-dependent same-material tribocharging in insulating grains. Phys Rev Lett 112(21):218001

Wang ZL (2017) On Maxwell's displacement current for energy and sensors: the origin of nanogenerators. Mater Today 20(2):74–82

Wang Z, Cheng L, Zheng Y, Qin Y, Wang ZL (2014a) Enhancing the performance of triboelectric nanogenerator through prior-charge injection and its application on self-powered anticorrosion. Nano Energy 10:37–43

Wang S, Xie Y, Niu S, Lin L, Liu C, Zhou YS, Wang ZL (2014b) Maximum surface charge density for triboelectric nanogenerators achieved by ionized-air injection: methodology and theoretical understanding. Adv Mater 26(39):6720–6728

Wang SH, Zi YL, Zhou YS, Li SM, Fan FR, Lin L, Wang ZL (2016) Molecular surface functionalization to enhance the power output of triboelectric nanogenerators. J Mater Chem A 4(10): 3728–3734

Wang J, Wu C, Dai Y, Zhao Z, Wang A, Zhang T, Wang ZL (2017) Achieving ultrahigh triboelectric charge density for efficient energy harvesting. Nat Commun 8(1):88

Willatzen M, Lew Yan Voon LC, Wang ZL (2020) Quantum theory of contact electrification for fluids and solids. Adv Funct Mater 30(17):1910461

Wu J, Wang X, Li H, Wang F, Yang W, Hu Y (2018) Insights into the mechanism of metal-polymer contact electrification for triboelectric nanogenerator via first-principles investigations. Nano Energy 48:607–616

Xu C, Zi Y, Wang AC, Zou H, Dai Y, He X, Wang P, Wang Y-C, Feng P, Li D, Wang ZL (2018) On the electron-transfer mechanism in the contact-electrification effect. Adv Mater 30(15):1706790

Zhang R, Olin H (2020) Material choices for triboelectric nanogenerators: a critical review. EcoMat 2(4):e12062

Zhang L, Cheng L, Bai S, Su C, Chen X, Qin Y (2015) Controllable fabrication of ultrafine oblique organic nanowire arrays and their application in energy harvesting. Nanoscale 7(4):1285–1289

Zhao J, Zhen G, Liu G, Bu T, Liu W, Fu X, Zhang P, Zhang C, Wang ZL (2019a) Remarkable merits of triboelectric nanogenerator than electromagnetic generator for harvesting small-amplitude mechanical energy. Nano Energy 61:111–118

Zhao G, Zhang Y, Shi N, Liu Z, Zhang X, Wu M, Pan C, Liu H, Li L, Wang ZL (2019b) Transparent and stretchable triboelectric nanogenerator for self-powered tactile sensing. Nano Energy 59: 302–310

Zheng Y, Cheng L, Yuan M, Wang Z, Zhang L, Qin Y, Jing T (2014) An electrospun nanowire-based triboelectric nanogenerator and its application in a fully self-powered UV detector. Nanoscale 6(14):7842–7846

Zhou YS, Liu Y, Zhu G, Lin Z-H, Pan C, Jing Q, Wang ZL (2013) In situ quantitative study of nanoscale triboelectrification and patterning. Nano Lett 13(6):2771–2776

Zi Y, Niu S, Wang J, Wen Z, Tang W, Wang ZL (2015) Standards and figure-of-merits for quantifying the performance of triboelectric nanogenerators. Nat Commun 6:8736

Zi Y, Guo H, Wen Z, Yeh M-H, Hu C, Wang ZL (2016) Harvesting low-frequency (<5 Hz) irregular mechanical energy: a possible killer application of triboelectric nanogenerator. ACS Nano 10(4):4797–4805

Zou H, Zhang Y, Guo L, Wang P, He X, Dai G, Zheng H, Chen C, Wang AC, Xu C, Wang ZL (2019) Quantifying the triboelectric series. Nature. Communications 10(1):1427